INVESTIGATION OF 2D AND 3D BOUNDARY-LAYER DISTURBANCES FOR ACTIVE CONTROL OF LAMINAR SEPARATION BUBBLES

Kai Augustin*, Ulrich Rist† and Siegfried Wagner ‡
Institut für Aerodynamik und Gasdynamik,
Universität Stuttgart, D-70550 Stuttgart, Germany

In the present paper mechanisms exploiting hydrodynamic instability of a laminar baseflow in order to control the size of a separation bubble are investigated in detail by means of 2D and 3D direct numerical simulations (DNS). An actuator introduces low amplitude Tollmien-Schlichting like boundary-layer disturbances into the flow upstream of the bubble, which become amplified and trigger early laminar-turbulent transition of the separated shear flow. In addition to a sinusoidal disturbance type, unsteady signals of shear-stress sensors downstream of the separation bubble are used as feedback input to the actuator. Within these simulations an easy to implement separation-bubble criterion to detect a region of separated flow based on shear stress sensors is used.

Nomenclature

C	Coefficient
F	Fourier coefficient
$\hat{L}$	Reference length, $[m]$
N	Set of points
Re	Reynolds number
T	Temporal period of the fundamental disturbance mode
U	Complex streamwise velocity amplitude
$\hat{f}$	Frequency, $[Hz]$
h	Temporal harmonic mode
k	Spanwise spectral mode
l	Timestep index
t	Temporal coordinate
u, v, w	Non-dimensional velocities
x, y, z	Non-dimensional cartesian coordinates
α	Streamwise wavenumber
β	Frequency parameter
γ	Spanwise wavenumber
δ_1	Displacement thickness
λ	Wavelength
$\hat{\nu}$	Kinematic viscosity, $[m^2/s]$
ω	Vorticity vector
$\omega_x, \omega_y, \omega_z$	Vorticity components
$\tilde{\Delta}$	Modified Laplace operator
Ψ	Stream function
Ψ_0	Separation streamline

Subscripts

L	With respect to the reference length
UB	At the free-stream boundary
k	Spanwise mode
n	Discrete streamwise coordinate
$wall$	At the wall
x	Streamwise direction
y	Wall-normal direction
z	Spanwise direction
δ_1	With respect to the displacement thickness
∞	Free-stream

Superscripts

$\hat{}$	Metric dimensional parameters
$'$	Disturbance parameters

Introduction

SEPARATION occurs in laminar boundary-layers at low Reynolds numbers due to the presence of strong adverse pressure gradients (APG). Boundary-layer disturbances become amplified by several orders of magnitude in the separated flow which leads to laminar-turbulent transition and re-attachment of the now turbulent flow, thus forming a laminar separation bubble (LSB). In the area of reverse flow in between separation and re-attachment the skin-friction is considerably lowered, but the LSB influences the pressure distribution of the whole airfoil and causes a thick wake resulting in an undesired overall drag increase. To maintain drag characteristics of an airfoil at low Reynolds numbers, the formation of LSBs has to be avoided.

*Research Engineer
†Senior Research Scientist
‡Professor, member AIAA

For this purpose drag reduction of low Reynolds number airfoils like airfoils with natural laminar flow of sail planes, wind energy turbine blades, or high lift devices like slats on commercial aircraft has to focus on reducing the size of the LSB while keeping the laminar trajectory of the flow as long as possible to avoid the generation of an additional drag penalty. Existing systems to avoid the formation of LSBs can generally be divided into "passive" or "active" systems, where "active" means that external energy has to be provided to influence the LSB either electrically or mechanically. Most of the mechanisms involve the generation of artificial turbulence in the laminar regime of the flow upstream of the separation. The momentum-rich turbulent flow is able to overcome the APG without separating. The often-used passive turbulators apply zig-zag or dimple tape mounted on the surface of the airfoil, but other designs have been used as well.[1] Less frequently used active devices use constant blowing of air through holes in the surface of the airfoil to generate large amplitude streamwise vortices. For these kinds of active devices a complicated system to provide the necessary bleed air has to be installed. All uncontrolled systems have in common that they have to be developed for an optimum design point and therefore can not capture off-design conditions, like speed tasks of sail planes optimized for thermal flights. Active blowing devices can be switched off at off-design conditions, but nevertheless additional disturbances are generated by secondary flow through the holes caused by pressure gradients along the airfoil.

More advanced active systems generate oscillations to control separation by either applying periodic suction and blowing via synthetic jets or use piezoelectric actuators[2,3] like MEMS or aerodynamic flow control (AFC). Those devices have been used successfully to control laminar and turbulent separation. Another approach to active control is to periodically deform the otherwise smooth top surface layer of the airfoil. Applied to laminar flow, which is very sensitive to surface roughness, those systems do not induce additional drag when switched off. As a drawback, these systems only provide very small deformation amplitudes, in order be low energy consuming, and imply electric driving and control devices. Moreover, a complex integrated sensor, controller and actuator system becomes desirable to make any external interference with the system by the pilot redundant. As a further constraint, most of the active turbulators have to be thin layered to fit into the limited space available on an airfoil besides the required supporting structural components.

Surface-bound active devices can generate high frequency perturbations. Sinha[4] suggests a system using active flexible wall (AFW) transducers, to control separated flow from the vicinity of the separation by so called micro-flexural wall vibrations combining sensors and actuators. The mechanism, which is investigated numerically in detail in the present paper applies to laminar flow only and involves the generation of Tollmien-Schlichting-like boundary-layer disturbances. Due to hydrodynamic instability of the separation-bubble flow, these boundary-layer disturbances become strongly amplified and this leads to laminar-turbulent transition despite the low initial disturbance amplitude. By introducing those boundary-layer perturbations at a disturbance strip upstream of the separation, transition can be triggered and therefore the size of the LSB be influenced.

In order to evaluate control methods using different disturbance forms and their impact on the size of a mid-chord LSB, 2D and 3D laminar separation-bubble flows are investigated in detail by means of direct numerical simulations (DNS).

Numerical Model

To study laminar separation bubbles, spatial DNS of a flat-plate boundary layer with a 2D baseflow are performed. An APG is applied locally at a certain distance from the inflow at the free-stream boundary to force separation. The code used for the present DNS has been used in different research programs for the investigation of transitional boundary layers with or without separation.[5–7] Fig. 1 shows a sketch of the rectangular integration domain.

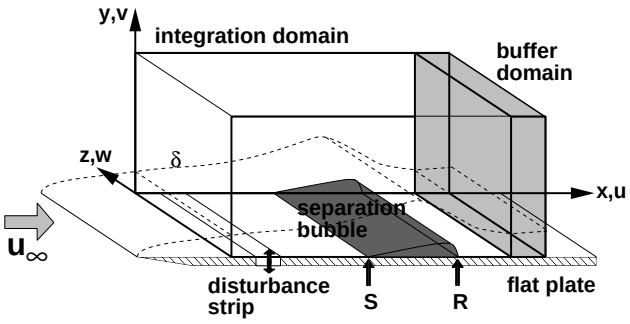

Fig. 1 3D integration domain with separation bubble and disturbance strip. 'S' marks the point of separation and 'R' the point of re-attachment.

All variables are non-dimensionalized by the free-stream velocity $\hat{u}_\infty = 30\ m/s$, a reference length $\hat{L} = 0.05\ m$ and the kinematic viscosity $\hat{\nu} = 15 \cdot 10^{-6}\ m^2/s$. Thus a reference Reynolds number Re_L (eqn. 1) and a frequency β (eqn. 2), coordinates (eqn. 3), velocities (eqn. 4), and a modified Laplace operator (eqn. 5) can be derived. In the simulations all wall-normal variables are stretched by a constant factor $\sqrt{Re_L}$.

$$Re_L = \frac{\hat{u}_\infty \hat{L}}{\hat{\nu}} \tag{1}$$

$$\beta = \frac{2\pi\ \hat{f}\ \hat{\nu}\ Re_L}{\hat{u}_\infty^2} \tag{2}$$

$$x = \frac{\hat{x}}{\hat{L}} \quad y = \sqrt{Re_L}\frac{\hat{y}}{\hat{L}} \quad z = \frac{\hat{z}}{\hat{L}} \tag{3}$$

$$u = \frac{\hat{u}}{\hat{u}_\infty} \quad v = \sqrt{Re_L}\frac{\hat{v}}{\hat{u}_\infty} \quad w = \frac{\hat{w}}{\hat{u}_\infty} \tag{4}$$

$$\tilde{\Delta} = \frac{1}{Re_L}\frac{\partial^2}{\partial x^2} + \frac{\partial^2}{\partial y^2} + \frac{1}{Re_L}\frac{\partial^2}{\partial z^2} \tag{5}$$

The complete Navier-Stokes equations for incompressible flows are solved in a vorticity-velocity formulation (6).

$$\frac{\partial \omega}{\partial t} - \nabla \times (\mathbf{v} \times \omega) = \tilde{\Delta}\omega \tag{6}$$

$$\text{with} \quad \mathbf{v} = \{u, v, w\} \quad \text{and} \quad \omega = -\nabla \times \mathbf{v} \tag{7}$$

Once the vorticity-transport equations are solved the remaining velocity components can be computed from three Poisson equations (8, 9, 10).

$$\frac{\partial^2 u}{\partial x^2} + \frac{\partial^2 u}{\partial z^2} = -\frac{\partial \omega_y}{\partial z} - \frac{\partial^2 v}{\partial x \partial y} \tag{8}$$

$$\tilde{\Delta} v = \frac{\partial \omega_x}{\partial z} - \frac{\partial \omega_z}{\partial x} \tag{9}$$

$$\frac{\partial^2 w}{\partial x^2} + \frac{\partial^2 w}{\partial z^2} = \frac{\partial \omega_y}{\partial x} - \frac{\partial^2 v}{\partial y \partial z} \tag{10}$$

These equations have been derived from the vorticity definition (7) and the continuity equation (11).

$$\frac{\partial u}{\partial x} + \frac{\partial v}{\partial y} + \frac{\partial w}{\partial z} = 0 \tag{11}$$

In order to get high-quality results from the simulation the correct computation of the vorticity at the wall becomes crucial. For the calculation of the three vorticity components at $y = 0$ the following three equations (12, 13, 14) are solved.

$$\frac{\partial^2 \omega_x}{\partial x^2} + \frac{\partial^2 \omega_x}{\partial z^2} = -\frac{\partial^2 \omega_y}{\partial y \partial x} + \frac{\partial}{\partial z}\tilde{\Delta} v \Big|_{y=0} \tag{12}$$

$$\omega_y = 0 \mid_{y=0} \tag{13}$$

$$\frac{\partial \omega_z}{\partial x} = \frac{\partial \omega_x}{\partial z} + \tilde{\Delta} v \Big|_{y=0} \tag{14}$$

A 4^{th}-order accurate numerical method is applied in time and space by finite differences in streamwise and wall-normal direction and by a four-step explicit Runge-Kutta scheme in time. For the spanwise direction a spectral ansatz (15) implying periodic boundary conditions is used.

$$f(x, y, z, t) = \sum_{k=-K}^{K} F_k(x, y, t) \cdot e^{ik\gamma z}, \quad \gamma = \frac{2\pi}{\lambda_z} \tag{15}$$

Due to this spectral ansatz, the Poisson equations for the streamwise and spanwise velocities reduce to ordinary differential equations. The remaining Poisson equation (9) for the wall-normal velocity is solved by a line-relaxation method accelerated by a non-linear multigrid algorithm. All Poisson equations can be solved separately for each spanwise spectral mode k allowing effective parallelization on shared memory computers using OpenMP. At the inflow boundary, a Blasius boundary-layer similarity solution with a momentum thickness Reynolds number $Re_{\delta_1} = 1722$ is prescribed. Considering the distance from the leading edge of the flat plate and a Blasius boundary-layer, this corresponds to an inflow Reynolds number $Re_{x_0} = 1.001 \cdot 10^6$. To avoid non-physical reflections at the outflow boundary, the disturbance amplitudes are artificially damped in a buffer domain[8] by several orders of magnitude.

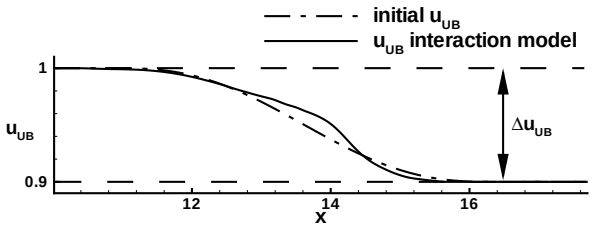

Fig. 2 Streamwise velocity u_{UB} at the free-stream boundary at the beginning of the calculation and as developed by the interaction model

The inviscid flow at the free-stream upper boundary is decelerated by 10% of $\hat{u}_\infty$ as shown in fig. 2. The displacement effects of the LSB on the potential flow are captured by a viscous-inviscid boundary-layer interaction model[7,9] at every timestep of the calculation. From the interaction model the characteristic "pressure plateau" in the u-velocity distribution develops with a constant velocity in the upstream part of the separation bubble and a sharp velocity drop in the region of the transition and re-attachment. A no-slip boundary condition is applied at the surface of the plate. At the disturbance strip, arbitrary 2D and 3D boundary-layer disturbances can be introduced into the flow by suction and blowing at the wall upstream of the LSB. The streamwise length of the disturbance strip has been set to one wavelength λ_x of the most amplified disturbance mode according to linear stability theory (LST)[10] and the beginning is located two wavelengths λ_x downstream of the inflow.

For the total streamwise length of the integration domain 18.41 wavelengths λ_x have been used. The height corresponds to 16 boundary-layer displacement thicknesses δ_1 at the inflow.

Disturbance Development

To successfully control the size of a LSB via the adjustment of the transition location, knowledge of the influence of different parameters of the boundary-layer disturbances on the separation bubble is required. This includes insight into the stability mechanisms of

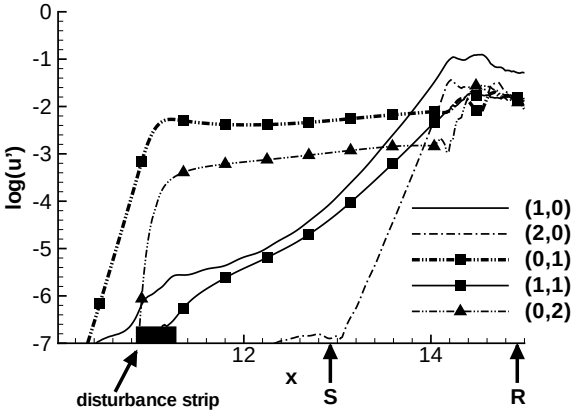

a) Steady 3D case.

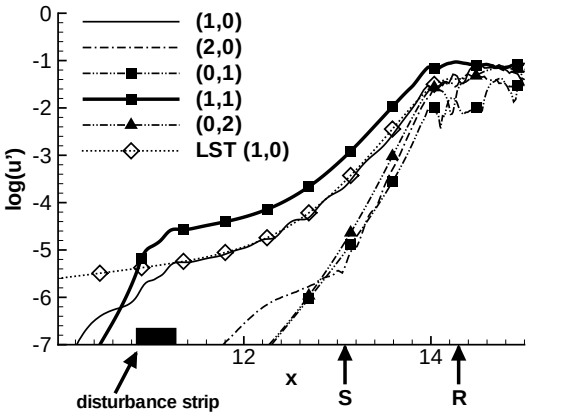

b) Oblique unsteady 3D case.

Fig. 3 Amplification of the disturbance velocity u' of 2D and 3D disturbances for the a) steady case and the b) oblique unsteady case.

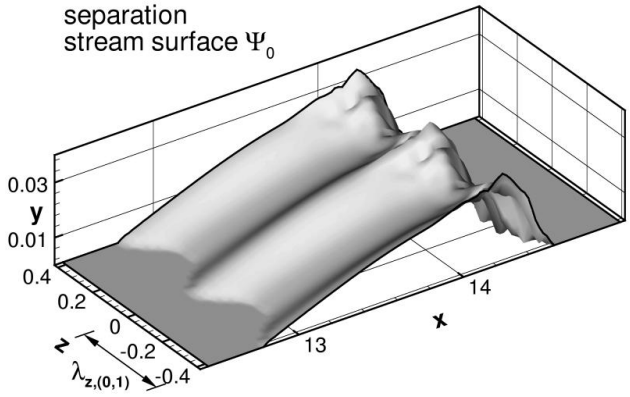

a) Steady 3D case.

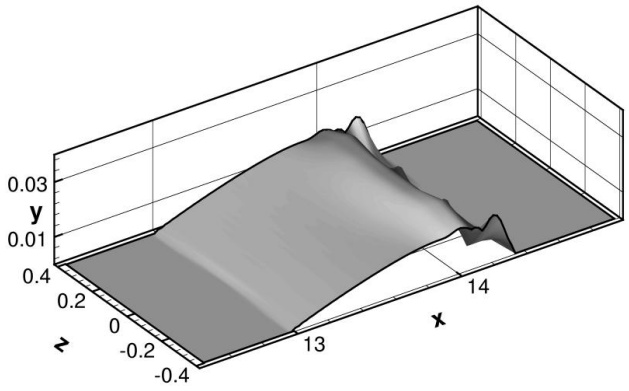

b) Oblique unsteady 3D case.

Fig. 4 Separation stream surface Ψ_0 for the a) steady case and the b) oblique unsteady case.

the base flow and into the resulting amplification or damping effect on boundary-layer disturbances. As a constraint, these properties have to be used to minimize the necessary kinetic energy to be introduced into the flow by the actuator. For these investigations, a mid-chord bubble case described in much detail by Rist[11] is used.

Earlier 2D investigations using DNS and linear stability theory[5,12] have already successfully influenced separation bubbles with pure 2D disturbances. Considering the fact that 3D steady disturbances can be generated much easier in practice, the development of steady 3D and weakly oblique unsteady 3D disturbances have been studied. The unsteady 3D disturbance modes have been compared to the pure 2D disturbance ones as well (which are very difficult to generate in real flow), whether they have a comparable effect on the size of the bubble.

Primary parameters for the specification of 3D disturbances are amplitude v'_0, frequency β and their streamwise and spanwise wavenumbers α and γ, respectively. The results show a different behavior of the LSB with respect to steady and unsteady disturbances. Fig. 3 compares amplification curves of the disturbance velocity u' versus x for different 2D and 3D spectral modes in logarithmic scale. The position of the disturbance strip as well as the points of separation 'S' and re-attachment 'R' are marked.

Steady 3D Case

In the first case a steady 3D disturbance mode (0,1) (bold dash-dot-dotted line with squares in fig. 3(a)) is excited at the disturbance strip with a wall-normal amplitude of $v'_{(0,1)} = 10^{-3}$. Further on, this case will be referred to as the "steady case". In the notation (h,k) the index h denotes harmonic modes with multiples of the fundamental frequency β (eqn. 2), while k means spectral modes of the spanwise wavenumber γ (eqn. 15). Thus (0,1) stands for a steady 3D disturbance with a spanwise wavelength $\lambda_z = 0.419$. Advancing in downstream direction, the disturbance amplitude of mode (0,1) is weakly damped at first and then weakly amplified far into the bubble. Only at $x \approx 14.2$ does it grow close to the point of non-linear saturation which marks the point of transition in this

case. A higher spanwise harmonic mode (0,2) (dash-dot-dotted line with deltas) is generated by non-linear interaction of the mode (0,1) with itself. At the disturbance strip an additional 2D mode (1,0) (solid line) of fundamental frequency has been excited to mimic background disturbances with an initial amplitude of $v'_{(1,0)} = 10^{-6}$, three orders of magnitude less than the amplitude of the 3D mode (0,1). This Tollmien-Schlichting mode is strongly amplified by base-flow instability and exceeds the amplitude of the 3D mode (0,1) at $x = 13.8$. It supersedes the steady mode (0,1) as the most dominant disturbance. An oblique fundamental mode (1,1) is generated by nonlinear interaction of the (1,0) and (0,1) modes continuously and finally reaches the amplitude of the 3D steady mode also. The whole scenario is dominated by unsteady 2D effects and three dimensionality plays only a minor role. Fig. 4(a) shows the 3D modulation of the separation stream surface Ψ_0 with the spanwise wavelength of mode (0,1), as marked by $\lambda_{z,(0,1)}$, of the otherwise 2D LSB. The separation stream surface Ψ_0 is defined as the value of the y-coordinate where the stream function $\Psi = \Psi(x, y, z)$ becomes zero.

Purely Oblique Unsteady 3D Case

In a second scenario, a pair of oblique (10°) unsteady modes [(1,1) and its symmetric counterpart (1,-1)], shown as a bold solid line with squares in fig. 3(b), is introduced into the same base flow as before. This case will be referred to as the "oblique unsteady case". The initial disturbance amplitude of mode (1,1) has been set to $v'_{(1,1)} = 10^{-5}$ at the wall. Fig. 3(b) shows the disturbance development in this second case. Again an unsteady 2D background disturbance (1,0) (solid line) is also present with the same initial amplitude as before.

In contrast to the first case, the wall-forced unsteady Tollmien-Schlichting mode (1,1) is strongly amplified and continues to be the most dominant mode. Although equally amplified, the 2D mode (1,0) stays below the oblique one due to the lower initial amplitude. For verification purposes, the development of the 2D mode (1,0) is compared to linear stability theory. Due to its very low amplitude, always at least 50% lower than the amplitude of mode (1,1), the mode shows very good agreement with the theory even inside the LSB up to the point where the amplitude finally saturates. Because of the strong amplification of mode (1,1), non-linear stages of the disturbance development ($\approx 1\%\ \hat{u}_\infty$) are reached somewhat further upstream than in the "steady case" at $x = 14.0$. The point of laminar-turbulent transition, and thus the reattachment, is shifted upstream likewise. Fig. 4(b) emphasizes the difference to the "steady case" by the separation stream surface Ψ_0. Compared to the large one in Fig. 4(a) the LSB is much shorter, of lower height and only slightly modulated in spanwise direction. Additional simulations show that the bubble vanishes totally at an initial disturbance level of $v'_{(1,1)} = 10^{-3}$.

Comparison

The difference in size of the bubble can also be compared by the time and spanwise averaged separation streamlines $\overline{\Psi}_0$ in fig. 5.

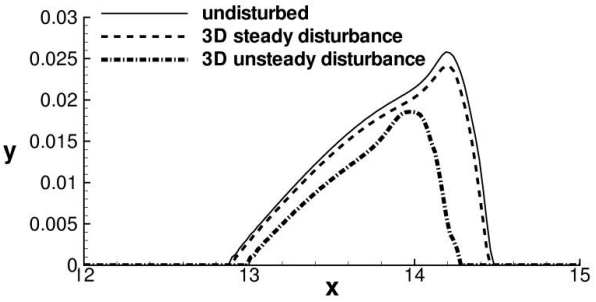

Fig. 5 Outline of the separation bubbles of the three different cases by the time and space averaged separation streamline $\overline{\Psi}_0$

The strong influence of unsteady modes is even more obvious here. Both cases are compared to an undisturbed third case (solid line), where only the small 2D background disturbance (1,0) with $v'_{(1,0)} = 10^{-6}$ is present in the flow. In the "steady case" (dashed line) the shape and size of the bubble merely differs from the undisturbed case, whereas in the "oblique unsteady case" (bold dash-dotted line) the height is only 72% and the length only 76% of the undisturbed bubble. This is valid despite the fact that the initial disturbance amplitude of the (0,1)-mode in the "steady case" is a hundred times larger than the amplitude of the (1,1)-mode in the "oblique unsteady case". This clearly shows the superiority of control scenarios using unsteady 2D[5] or weakly oblique 3D boundary layer disturbances compared to steady ones.

In fig. 6, two different amplification diagrams have been obtained from linear stability theory, where small disturbances are represented by (eqn. 16) with complex streamwise wavenumbers α and frequencies β (eqn. 17), and real spanwise wavenumbers γ.

$$u'(x, y, t) = U(y) \cdot e^{i(\alpha x + \gamma z - \beta t)} \tag{16}$$

$$\text{with} \quad \alpha = \alpha_r + i\alpha_i \quad \text{and} \quad \beta = \beta_r + i\beta_i \tag{17}$$

Negative α_i denote exponential spatial amplification, accordingly. Here the amplification rates are shown versus spanwise wavenumber γ and frequency β at a certain streamwise position x.

In both figures the region of maximum spatial amplification is located close to $\gamma = 0$, i.e. 2D flow. For higher spanwise wavenumbers, the amplification is reduced, whereas the region of amplified disturbance modes broadens when the LSB is approached in streamwise direction.

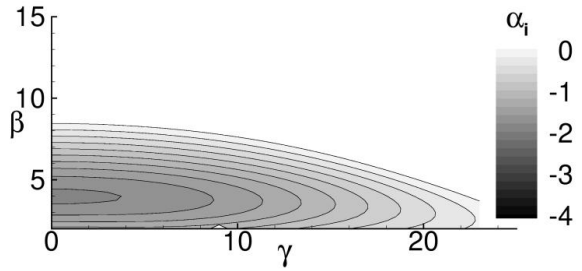

a) Amplification rates for $x = 12.048$

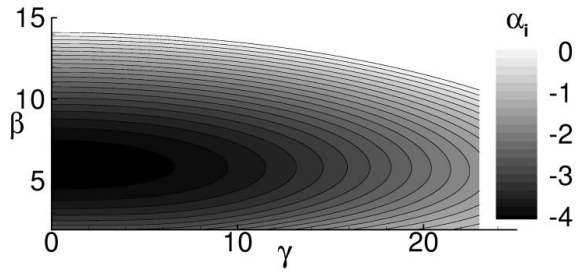

b) Amplification rates for $x = 12.83$

Fig. 6 Contours of the spatial amplification rate α_i versus spanwise wavenumber γ and frequency β at two different streamwise positions x

Spanwise wavenumber $\gamma = 15$ means 45° angle of obliqueness. This underlines that 2D and weakly 3D disturbance scenarios are more effective not only compared to steady ones, but also compared to scenarios using disturbance modes with higher angles of obliqueness.

Skin-Friction Signal Feedback

The above results show the advantages of using unsteady 2D or 3D disturbances rather than steady disturbances. In order to provide the necessary unsteady disturbance amplitude, the system can be extended by a signal feedback mechanism, where instantaneous amplitude signals of the skin-friction downstream of the disturbance strip provide unsteady input to the actuator.

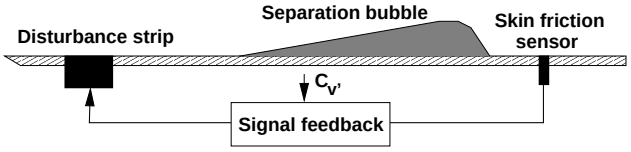

Fig. 7 Sketch of the skin-friction signal feedback mechanism

$$v_0'(t_l) = C_{v'} \cdot \omega_{z,wall}(x_n, t_{l-1}) \tag{18}$$

The feedback mechanism as applied in the simulation is sketched in fig. 7 and can be described by equation (18), where instantaneous skin-friction data from a previous timestep $l-1$ at a certain streamwise position x_n is used as the forcing amplitude signal v_0' at the disturbance strip of the current timestep l. Due to

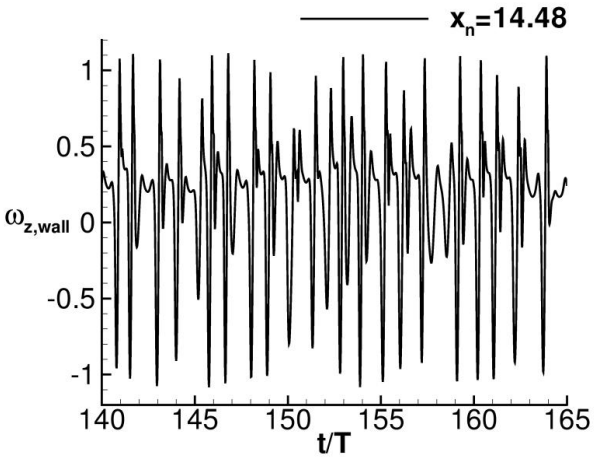

Fig. 8 Time trace of $\omega_{z,wall}$ at the sensor position

the above mentioned fact that 2D or weakly 3D disturbances are most effective in influencing the LSB, 2D DNS have been performed to investigate the properties of the suggested feedback mechanism. To gain the desired amplitude level, the amplitude is multiplied by an arbitrary factor $C_{v'}$, which can also be set automatically by a controller according to a detected length of a separation bubble. As a broad spectrum of disturbance frequencies becomes desirable, data from the quasi turbulent flow downstream of the re-attachment can be used. Initially, the flow has been disturbed by a background perturbation of the fundamental mode (1,0) of frequency $\beta = 5$ and $v'_{(1,0)} = 10^{-6}$ for a startup period of 120 cycles (T). Although the fundamental disturbance period becomes nonrepresentional for the time scale, the time instance will still be indicated by multiples of the time period T after the feedback mechanism has been switched on at $t = 120T$. For the investigation of of the feedback mechanism, the boundary-layer interaction model has not been used. Therefore, the location of the LSB in this case is shifted downstream and the bubble is of lower height compared to the "natural case" in fig. 5. The skin-friction sensor has been placed at $x_n = 14.48$ about $1.15 \cdot \lambda_x$ of the fundamental disturbance (1,0) downstream of the re-attachment line. After the startup phase, the signal feedback has been turned on for 80 (pseudo-)periods T. Fig. 8 shows a time-trace of the skin-friction signal at $x_n = 14.48$ over $25T$.

Fig. 9 shows amplitude spectra of the skin-friction $\omega_{z,wall}$ in logarithmic scale. A timewise Fourier analysis of the interval $160T \leq t \leq 200T$ (to avoid the capturing of any transient effects from the startup of the feedback) clearly shows the broad spectrum of frequencies present in the flow. The solid line shows the amplitude spectrum at $x_n = 14.48$ where the sensor is located. Moreover, the first and second curve in fig. 9 show the resulting spectrum at the streamwise position $x_n = 11.3$ (line with triangles) and $x_n = 12.25$

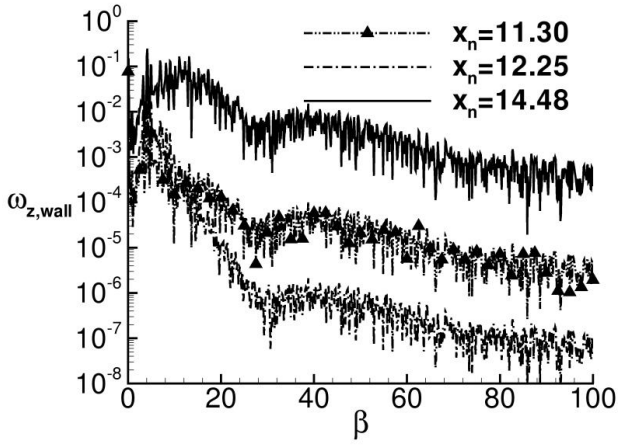

Fig. 9 Frequency spectra of the skin-friction $\omega_{z,wall}$ at three different streamwise positions

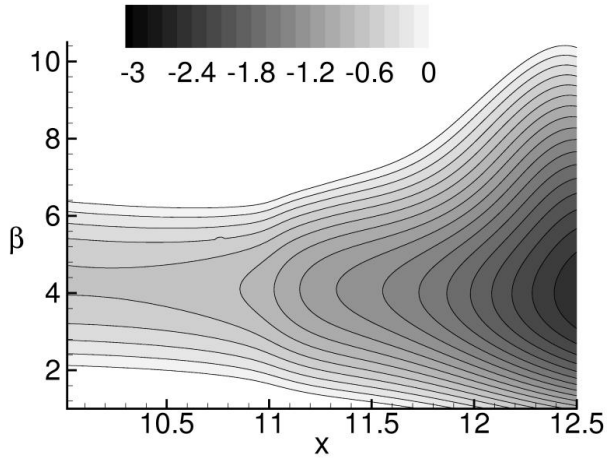

Fig. 10 Amplification rate α_i according to linear stability theory of the time averaged flow

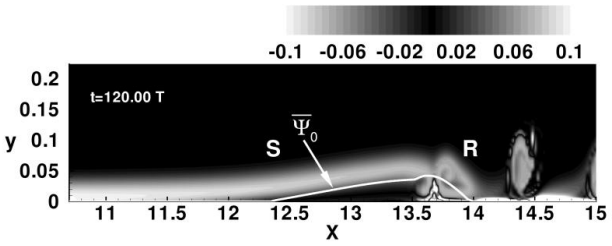

a) Disturbance Amplitude $v'_{(1,0)} = 10^{-6}$ at $t = 120T$

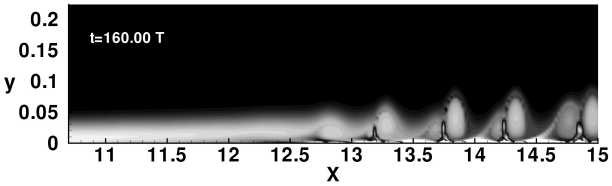

b) Disturbance Amplitude at $t = 160T$ from feedback at $x = 14.48$

Fig. 11 Comparison of the spanwise vorticity for two different amplitude levels and kinds of forcing

(dash-dotted line) a short distance downstream of the disturbance strip but upstream of the separation. The factor $C_{v'}$ has been set to $5 \cdot 10^{-3}$. As the level of the disturbance signal at $x_n = 14.48$ is of order 1, the chosen factor $C_{v'}$ compares to the disturbance level in fig. 3(a).

Amplitudes of disturbance frequencies, which are amplified or damped by the boundary-layer, can be distinguished from the two curves $x_n = 11.3$ and $x_n = 12.25$ in fig. 9. The streamwise position $x_n = 11.3$ is located only a short distance downstream of the end of the disturbance strip and therefore the curve almost represents the initial spectrum of the excited disturbance. The band of frequencies which are spatially damped or amplified in this domain can be obtained by comparing to the spectrum at $x_n = 12.25$. The dominant frequencies are located in the band between $\beta \approx 2$ and $\beta \approx 10$. All other frequencies are damped. These amplified frequencies agree well with the band of frequencies which are amplified according to LST. In fig. 10, contours of the amplification rate versus streamwise coordinate and frequency are plotted. Again, the amplified frequencies show negative amplification rates α_i.

Initially, only a narrow band of frequencies upstream of the separation is amplified, but, advancing in downstream direction, it widens and the amplification increases. In the separation bubble nonlinear effects set in, which lead to an even broader band of amplified frequencies and finally to laminar-turbulent transition.

The effectiveness of the feedback mechanism can be shown by the spanwise vorticity ω_z in fig. 11. Here, contours of the instantaneous vorticity are plotted versus streamwise and wall normal coordinates at two different timesteps of the calculation. At $t = 120T$ (fig. 11(a)), where only the small background disturbance is excited at the disturbance strip, a large separation bubble is present. The shape of the separation bubble is outlined by the time averaged separation streamline $\overline{\Psi}_0$. Applying the skin-friction signal feedback with the given factor $C_{v'}$, the transition location is shifted far upstream in fig. 11(b) which is taken $40T$ later. The transition location is marked by the onset of vortex shedding, which takes place much earlier compared to fig. 11(a). The time averaged separation streamline $\overline{\Psi}_0$ shows no detached flow in the case, where the feedback mechanism is used.

Fig. 12 provides a x–t–diagram with contours of the skin-friction $\omega_{z,wall}$ over $30T$ after the disturbance generation has been switched to skin-friction signal feedback. The separation bubble emerges as a white area at the lower end of the figure, whereas the region of higher skin-friction upstream and downstream of the bubble appears dark gray or black. Five T after the feedback has been switched on, the region of

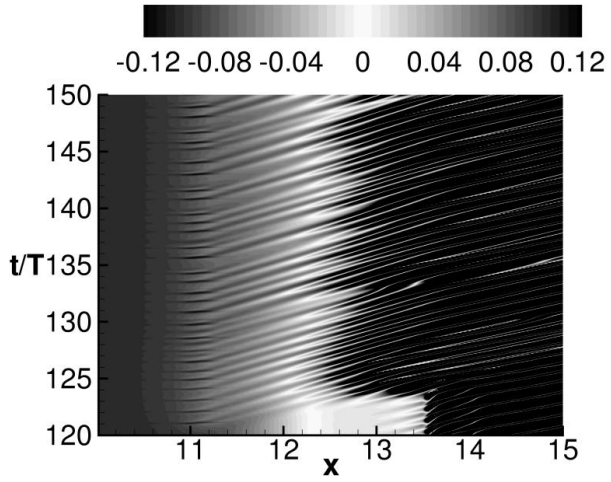

Fig. 12 x–t **diagram of the skin-friction** $\omega_{z,wall}$

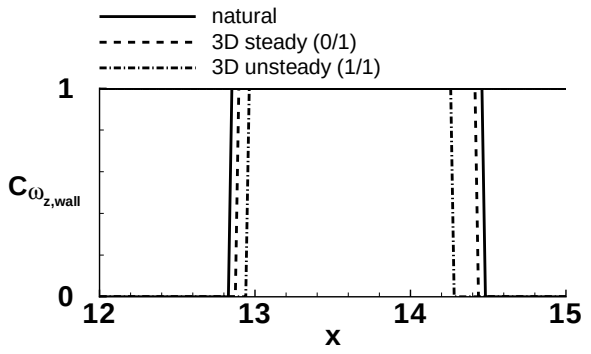

Fig. 13 Extent of the separation bubbles of the three different cases as detected by the binary bubble criterion $c_{\omega_{z,wall}}(x)$**.**

strong positive skin-friction is shifted almost instantly to $x = 12.5$. The onset of vortex shedding, traced by oblique lines of alternating bright and dark shades, is being shifted upstream to $x = 11$, as well. A region of evenly distributed negative skin-friction, the LSB, is not present any more. After the new flow pattern has been established, an almost constant vortex shedding frequency sets in, despite some irregularities, e.g. in $130T \leq t \leq 135T$ due to the properties of the feedback signal (cf. fig. 8). This data shows that the transitional phase, where the re-attachment moves upstream, is very short once the disturbances caused by applying the feedback mechanism have been convected into the LSB.

Separation Bubble Detection

Another focus, beside the identification of optimum disturbance modes, is the identification of the bubble by a sensor system and a criterion which facilitates control of the LSB. One way to determine the length of a LSB is based on the time averaged skin-friction $\omega_{z,wall}$. Because of the laminar state of the flow, the separation line is easy to detect from the skin-friction whereas the re-attachment line is hidden in a region of strong gradients of $\omega_{z,wall}$ due to the vortex shedding in the turbulent rear part of the separation bubble (cf. fig. 12.). The difference in the amplitudes of the skin-friction makes the detection of the re-attachment even more complicated. Because of the high positive amplitudes and the only weak negative amplitudes in the vicinity of the re-attachment, the time averaged data is still dominated by the high positive amplitudes, even if positive amplitudes are equal or less frequent than the negative ones. This makes the re-attachment line very hard or impossible to determine correctly from time averaged data.

To resolve this problem, one can use histograms, which do not show the dependency on gradients or amplitude differences, of the spanwise skin-friction at discrete streamwise positions x_n to derive a clearer and easy-to-implement bubble detection criterion.[13]

If the number N of points with $\omega_{z,wall}$ values less than zero exceeds the number of points with $\omega_{z,wall}$ values larger than zero, the considered streamwise position lies within the separated region. These properties can be used to define the binary separation bubble criterion as

$$C_{\omega_{z,wall}}(x_n) = \begin{cases} 1 & N_{\omega_{z,wall}<0} \leq N_{\omega_{z,wall}>0} \\ 0 & N_{\omega_{z,wall}<0} > N_{\omega_{z,wall}>0} \end{cases}, \tag{19}$$

which becomes 1 for points located inside the bubble and 0 for all other streamwise points. Applied to the above "natural case", the "steady case" and the "oblique unsteady case", the extension of the respective LSB can be confidently determined by the above criterion (compare fig. 5 and fig. 13). However, a shortcoming of this easy-to-use method is that only the streamwise extent but not the height of the LSB becomes accessible for the control of the bubble. A flat separation bubble can become desirable because of the low skin-friction inside the LSB leading to reduced total drag. Nevertheless, the bubble criterion is well suited for a controller which then changes the amplitude of the disturbance input or the amplitude factor $C_{v'}$ of the feedback input upstream, according to the criterion, and thus reduces the size of the LSB.

Conclusions

Laminar separation bubbles have been investigated by means of spatial direct numerical simulations of a flat-plate boundary-layer flow with an adverse pressure gradient applied locally. Different steady and unsteady boundary-layer disturbances were introduced at a disturbance strip upstream of the separation and their effects on the separation bubble have been studied. 2D or weakly 3D unsteady disturbances have a stronger impact on the size of the bubble than steady disturbances by utilizing the instability of the baseflow. An initial amplitude for an unsteady 2D or 3D disturbance two to three orders of magnitude less than the one for

a steady disturbance is sufficient to gain the same or an even larger effect on the LSB.

Beside artificially generated disturbances, instantaneous skin-friction signals taken from a position downstream of the separation bubble can be used as amplitude input to an actuator upstream of the bubble. The broad band of frequencies in the most unstable frequency range, according to linear stability theory, provide a robust signal source for the actuator, adjustable by an arbitrary amplification factor.

The influence of different kinds of disturbances on separation bubble control can confidently be evaluated by an easy-to-implement binary separation bubble criterion based on discrete values of the skin-friction. The criterion will be used as input for an active control mechanism for separation bubble flows.

Acknowledgments

Support from the Deutsche Forschungsgemeinschaft through grant Ri 690/11 is gratefully acknowledged. Computing time on NEC SX–4 and SX–5 computers has been provided by the Höchstleistungsrechenzentrum Stuttgart (HLRS) through the LAMTUR project. The author would like to thank Thomas Beisel (HLRS) and Holger Berger (NEC ESS) for their support when using some of the most recent computing platforms.

References

[1]Kerho, M., Hutcherson, S., Blackwelder, R. F., and Liebeck, R. H., "Vortex Generators Used to Control Laminar Separation Bubbles," *Journal of Aircraft*, Vol. 30, No. 3, 1993, pp. 315–319.

[2]Seifert, A., Eliahu, S., Greenblatt, D., and Wygnanski, I., "Use of Piezoelectric Actuators for Airfoil Separation Control," *AIAA Journal*, Vol. 36, No. 8, 1998, pp. 1535–1537.

[3]Munday, D., Jacob, J., and Huang, G., "Active Flow Control of Separation on a Wing with Oscillatory Chamber," *40th AIAA Aerospace Sciences Meeting and Exhibit*, No. 2002–0413, Reno, NV, USA, January 14-17 2002.

[4]Sinha, S. K., "Flow Separation Control with Microflexural Wall Vibrations," *Journal of Aircraft*, Vol. 38, No. 3, May-June 2001, pp. 496–503.

[5]Rist, U., Augustin, K., and Wagner, S., "Numerical Simulation of Laminar Separation Bubble Control," *Notes on Numerical Fluid Mechanics (NNFM)*, Vol. 77, 2001, pp. 170–177.

[6]Rist, U. and Fasel, H., "Direct Numerical Simulation of Controlled Transition in a Flat-Plate Boundary Layer," *J. Fluid Mech.*, Vol. 298, 1995, pp. 211–248.

[7]Maucher, U., *Numerische Untersuchungen zur Transition in der laminaren Ablöseblase einer Tragflügelgrenzschicht*, Dissertation, Universität Stuttgart, 2002.

[8]Kloker, M., Konzelmann, U., and Fasel, H., "Outflow Boundary Conditions for spatial Navier-Stokes Numerical Simulations of Transition Boundary Layers," *AIAA Journal*, Vol. 31, No. 4, 1993, pp. 620–628.

[9]Maucher, U., Rist, U., and Wagner, S., "Refined Interaction Method for Direct Numerical Simulation of Transition in Separation Bubbles," *AIAA Journal*, Vol. 38, No. 8, 2000, pp. 1385–1393.

[10]Reed, H., Saric, W. S., and Arnal, D., "Linear Stability Theory Applied to Boundary Layers," *Annu. Rev. Fluid Mech.*, Vol. 18, 1996, pp. 389–428.

[11]Rist, U., *Zur Instabilität und Transition in laminaren Ablöseblasen*, Habilitation, Universität Stuttgart, 1999, Shaker Verlag.

[12]Augustin, K., Rist, U., and Wagner, S., "Active Control of a Laminar Separation Bubble," *Notes on Numerical Fluid Mechanics (NNFM)*, Vol. 76, 2001, pp. 297–303.

[13]Augustin, K., Rist, U., and Wagner, S., "Active Control of Separation Bubbles Exploiting Laminar Baseflow Instabilities," *Proceedings of 2002 ASME-European FED Summer Annual Meeting*, No. 31047, Montreal, Quebec, Canada, July 14-18 2002.